Appl. Phys. A (2017) 123:761
DOI 10.1007/s00339-017-1391-6

Applied Physics A
Materials Science & Processing

Zr-doped SnO_2 thin films synthesized by spray pyrolysis technique for barrier layers in solar cells

N. Nanda Kumar Reddy[1] · Harish Sharma Akkera[2] · M. Chandra Sekhar[3] · Si-Hyun Park[3]

Received: 4 September 2017 / Accepted: 7 November 2017 / Published online: 11 November 2017

Abstract In the present work, we investigated the effect of Zr doping (0–6 at%) on the structural, electrical, and optical properties of tin oxide (SnO_2) thin films deposited onto glass substrates using a spray pyrolysis technique. The room-temperature X-ray diffraction pattern shows that all deposited films exhibit polycrystalline tetragonal structure. The pure SnO_2 film is grown along a preferred (200) direction, whereas Zr-doped SnO_2 (Zr:SnO_2) films started growing along the (220) orientation along with a high intensity peak of (200). Scanning electron microscope (SEM) and atomic force microscope (AFM) images showed that the grains of the films are spherical in structure, and the grain size decreased with increasing of Zr concentration. The optical transmission spectra of deposited films as a function of wavelength confirm that the average optical transmittance is > 85% for Zr:SnO_2 films. The value of the optical bandgap is significantly decreased from 3.94 to 3.68 eV with increasing Zr concentration. Furthermore, the electrical measurements found that the sheet resistance (R_{sh}) and resistivity (ρ) values are decreased with increasing of Zr doping. The lowest values of $R_{sh} = 6.82\ \Omega$ and $\rho = 0.4 \times 10^{-3}\ \Omega$ cm are found in 6-at% Zr-doped SnO_2 film. In addition, a good efficiency value of the figure of merit ($\phi = 3.35 \times 10^{-3}\ \Omega^{-1}$) is observed in 6-at% Zr-doped SnO_2 film. These outstanding properties of Zr-doped SnO_2 films make them useful for several optoelectronic device applications.

1 Introduction

In recent years, considerable interest has been growing to develop transparent metal oxide thin films owing to their potential applications in technological fields such as solar cells, electrochromic devices, photovoltaics, photocatalytic, gas sensors, and other optoelectronic devices [1–8]. Among the various transparent metal oxide thin films, tin oxide (SnO_2) is an appropriate candidate material owing to its high band-gap energy of 3.6–4.0 eV [9], high electrical conductivity, and high optical transmittance. In addition, SnO_2 thin films have higher chemical and mechanical stability compared with other transparent metal oxide thin films [10]. However, undoped SnO_2 thin film has low electrical conductivity owing to its intrinsically low carrier density and mobility. Hence, effective doping is one way to control the oxygen vacancies and improve the conductivity of SnO_2 with a suitable dopant.

Several authors used many dopants such as Ag, Al, Ga, Zn, In, Mn, Sb, and Ru in SnO_2 films to improve these properties [11–18]. Among these dopants, Zr can obtain a high quality of films for optoelectronic device applications [19]. Zr is a *n*-type material, and the Zr^{4+} ionic radius (0.79 Å) is larger than the Sn^{4+} ionic radius (0.69 Å) [20]. Hence, Zr^{4+} ions can easily replace Sn^{4+} ions in the crystal lattice, and the product compound can stabilize the lattice structure. Therefore, Zr is a perfect dopant to improve the optical and electrical characteristics of SnO_2 thin films for developing optoelectronic devices. Pure SnO_2 thin films

✉ M. Chandra Sekhar
chandu.phys@gmail.com

✉ Si-Hyun Park
sihyun_park@ynu.ac.kr

[1] Department of Physics, Madanapalle Institute of Technology and Science, Madanapalle, Andhra Pradesh 517325, India

[2] Department of Physics, Indian Institute of Science, Bangalore, Karnataka 560012, India

[3] Department of Electronic Engineering, Yeungnam University, 280 Daehak-ro, Gyeongsan-si, Gyeongsangbuk-do 3854, Republic of Korea

can be synthesized by various deposition techniques such as electron beam evaporation [21], magnetron sputtering [22], atomic layer deposition [23], chemical vapor deposition [24], and pulsed laser deposition [25]. Compared to the above techniques, spray pyrolysis is one of the best owing to its low cost, homogeneous growth on large-area substrates, and easy control of the chemical composition of thin film. In this study, we systematically explored the effects of Zr (0–6 at%) doping on the structural, electrical, and optical properties of SnO_2 films synthesized by the spray pyrolysis technique onto glass substrates.

2 Experimental

Pure SnO_2 and Zr-doped SnO_2 (Zr:SnO_2) films were deposited on glass substrate using the spray pyrolysis technique. To deposit the pure SnO_2 film, we used $SnCl_2{\cdot}2H_2O$ as the source material. It was dissolved in absolute ethanol (C_2H_5OH) by adding a few drops of HCl. To deposit the Zr-doped SnO_2 films (Zr:SnO_2), Zirconium(IV) acetylacetonate [$Zr(Acac)_4$, Sigma Aldrich, 99%] was used as the source for Zr doping. Different precursor solutions were prepared by adding Zr $(Acac)_4$ dopant to the source SnO_2 solution. The Zr concentrations in the SnO_2 spray solution ([Zr]/[Sn]) were 0, 1.5, 3, 4.5, and 6 at%, which are represented as Z0, Z1, Z2, Z3, and Z4, respectively. Commercially available quartz glass slides with an area of 1 cm × 1 cm and thickness of 1.3 mm, as the substrate, were cleaned with distilled water and organic solvents several times with deionized water, followed by an ultrasonic bath for 15 min, and then dried in an argon gas atmosphere.

The prepared solutions were sprayed on the glass substrates through a glass nozzle of 0.1-mm diameter using the air as a carrier gas. The distance between the nozzle and substrate was kept constant at 25 cm, and a uniform spray rate of 5 ml/min was maintained for 30 min for all films. Thus, all deposited films had almost the same thickness of about 600 ± 15 nm, as confirmed by a stylus profilometer. The temperature was kept at a constant 400 °C for all samples. The temperature was measured using a Chromel–Alumel thermocouple controlled by a digital proportional–integral–derivative (PID) temperature controller with an accuracy of ± 5 °C. A crystal structure analysis was conducted by grazing incidence X-ray diffraction (GIXRD) using a Rigaku X-ray diffractometer with CuK_α radiation having a wavelength $\lambda = 1.5406$ Å in the 2θ range from 10° to 70°. The deposited films were subjected to morphological characterization using a Zeiss Evo18 scanning electron microscope (SEM) and atomic force microscopy (AFM). The optical transmittance spectra were taken using a Shimadzu UV–visible spectrophotometer at room temperature. The electrical properties were measured with a Keithley measurement source unit using a four-probe method.

3 Results and discussion

Figure 1 depicts the XRD pattern of the pure SnO_2 (Z0) and Zr:SnO_2 (Z1, Z2, Z3, and Z4) films deposited onto glass substrates. The XRD results clearly indicate that all deposited films exhibited a tetragonal polycrystalline rutile structure. The fundamental diffraction peak (200), which is a higher intensity diffraction reflection, and the small-intensity super lattice peaks (110), (101), (211), and (220) are indexed. The observed peaks exactly match the standard ones from JCPDS card no. 41-1445 and belong to the space group P42/mm (number 136). The pure SnO_2 film (Z0) shows a preferred growth orientation along the (200). However, in Zr:SnO_2 films, the (220) peak intensity continuously increased as the Zr concentrate ion increased, and shows a slight change in the reorientation effect of the lattice planes. Babar et al. [26] and Turgut et al. [15] observed similar results in their studies. The lattice constants a and c for the tetragonal phase structure are calculated by the following equation [27]:

$$\frac{1}{d^2} = \left(\frac{h^2 + k^2}{a^2}\right) + \frac{l^2}{c^2}, \tag{1}$$

where d is the interplanar distance, and h, k, and l are Miller indices. The lattice constants for the tetragonal SnO_2 film were found to be $a = 4.7516$ Å and $c = 3.1844$ Å. Moreover,

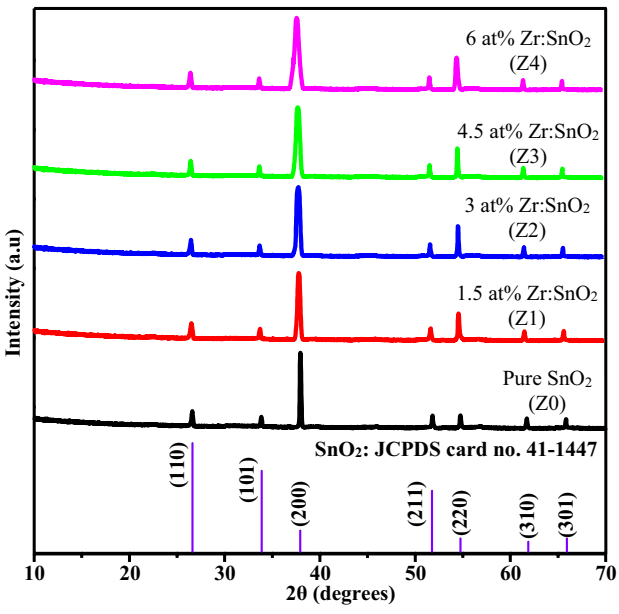

Fig. 1 XRD pattern of pure SnO_2 (Z0) and various concentrations (1.5, 3, 4.5, and 6 at%) of Zr-doped SnO_2 (Z1, Z2, Z3, and Z4) films

the lattice constants for the Zr-doped SnO_2 films (Z1, Z2, Z3, and Z4) were higher than that of the pure SnO_2 film. Values are listed in Table 1.

On the other hand, (200) fundamental peak broadening was observed as the Zr concentration increased. This indicates a decrease in grain size with an increase in Zr content, and is confirmed by the reduction in full-width at half-maximum (FWHM) with increasing Zr concentrations in SnO_2. In addition, an observed shift in (200) reflection toward a lower angle indicates an increase in the cell volume owing to a larger ionic radius of the Zr (0.72 Å) atom as compared to Sn (0.68 Å). The average grain size (D) of all deposited polycrystalline films (Z0, Z1, Z2, Z3, and Z4) was calculated using the Debye–Scherrer formula [28], and the corresponding values are given in Table 1.

$$D = \frac{0.9\lambda}{\beta cos\theta}, \tag{2}$$

where D is the grain size of the nanoparticles, β is the full-width at half of the peak maximum (FWHM) in radians, and θ is Bragg's angle. The measured grain size values for the (200) peaks are given in Table 1. For the (200) peak, the calculated D values continuously decrease from 49 to 14 nm with an increase in the Zr concentration, which suggests that additional Zr distracts the SnO_2 lattice owing toan increase in the number of nucleation centers. The mismatch microstrain (ε) is one of the most important factors in nanostructured thin films, and can unfavorably affect the structural properties. It can be calculated from the geometric mismatch between the crystalline lattices of the thin films and the substrate [29]. The microstrain (ε) values of pure SnO_2 (Z0) Zr:SnO_2 (Z1, Z2, Z3, and Z4) films for the (200) peaks are measured by the following formula [30]:

$$\varepsilon = \left(\frac{1}{\sin\theta}\right)\left[\left(\frac{\lambda}{D}\right) - (\beta\cos\theta)\right], \tag{3}$$

where β is the full-width at half-maximum of the preferred peak, and D is the average grain size. The calculated values are given in Table 1. For the (200) peak, the microstrain (ε) increases with an increase in Zr concentration.

Figure 2 depicts the scanning electron microscope (SEM) and atomic force microscope (AFM) microstructures of the pure SnO_2 (Z0) and Zr:SnO_2 (Z1, Z2, Z3, and Z4) films. The SEM and AFM images show that the Zr concentration effectively changes the microstructure of the films. All deposited films were homogeneous and free of cracks. Both the SEM and AFM microstructures replicate a decrease in grain size with an increase in Zr content, and are also in good agreement with the XRD results. The average grain size values measured by FESEM (Fig. 2Ia–e) for the films Z0, Z1, Z2, Z3, and Z4 were found to be 70 ± 2, 52 ± 3, 46 ± 3, 35 ± 3, and 21 ± 3 nm, respectively. The observed grain size values from SEM

Table 1 Various parameters for pure SnO_2, and Zr-doped SnO_2 thin films

Sample name	Zr concentration (at%)	Lattice parameters (nm)		Cell volume $(nm)^3$	Grain size (nm)			Microstrain $(\varepsilon) \times 10^{-3}$	Figure of merit $(\phi) \times 10^{-3}$ (Ω^{-1})	Average roughness (R_{avg}) (nm)	Sheet resistance (R_{sh}) (Ω)	Resistivity $(\rho) \times 10^{-3}$ $(\Omega$ cm)
		a	c		XRD	SEM	AFM					
Z0	0	4.7516	3.1844	71.8964	49	70 ± 2	74 ± 3	1.0689	0.23	11.23	88.4	5.30
Z1	1.5	4.7641	3.2014	72.6611	25	52 ± 3	56 ± 3	1.8827	0.98	8.64	56.3	3.39
Z2	3	4.7724	3.2159	73.2447	20	46 ± 3	48 ± 2	2.2646	0.36	6.12	32.6	1.95
Z3	4.5	4.7865	3.2174	73.7125	18	35 ± 3	39 ± 3	2.5595	1.23	3.84	14.5	0.87
Z4	6	4.8023	3.2186	74.2276	14	21 ± 3	23 ± 3	3.3702	3.35	2.16	6.8	0.40

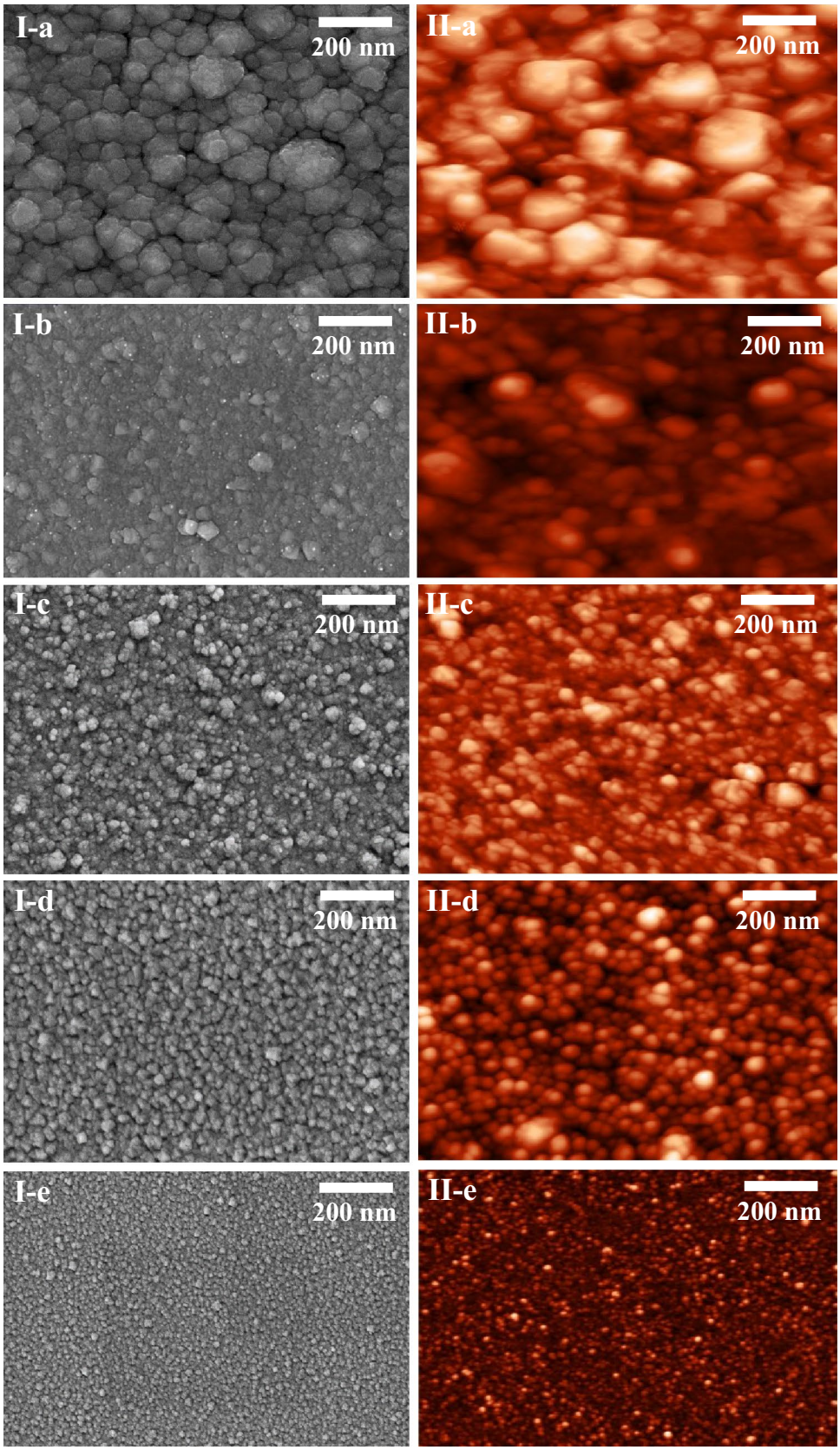

Fig. 2 Ia–e SEM images and IIa–e AFM images of pure SnO_2 (Z0) and various concentrations (1.5, 3, 4.5, and 6 at%) of Zr-doped SnO_2 (Z1, Z2, Z3, and Z4) films

and AFM (Fig. 2IIa–e) are moderately similar, as shown in Fig. 2.

However, the overall grain sizes shown by SEM and AFM are much larger than those shown by XRD. This is ascribed to the fact that SEM and AFM show agglomerations of the particles, whereas XRD gives an average grain size [31]. The average surface roughness of the films plays a vital role in developing optoelectronic devices [32]. The average surface roughness not only describes the light scattering, but also gives an idea of the quality of the surface under investigation. For a quantitative evaluation of the surface topography, the average surface roughness (R_{avg}) was measured from AFM scans over film areas of 1×1 µm in semi-contact mode. Three scans in different areas were conducted for each sample using the following equation [33]:

$$R_{avg} = \frac{1}{N}\sum_{i=1}^{N}\left|Z_i - \overline{Z}\right|, \tag{4}$$

where N is the number of surface height data, and $\overline{Z}$ is the mean height distance. AFM topography tells us that the average surface roughness (R_{avg}) decreases as the Zr concentration increases. The values are listed in Table 1.

Figure 3 shows the optical transmittance curves determined in a wavelength range of 300–800 nm for pure SnO_2 (Z0) and Zr:SnO_2 (Z1, Z2, Z3, and Z4) films measured with a UV–visible spectrometer. It can be found that the average transmittance is greater than 80% for all films in the visible and near-infrared regions. This indicates that Zr-doped SnO_2 films are highly transparent and can be used for window layers for solar cells. However, the average transmittance decreases from 90 to 80% as the Zr concentration increases.

In the present study, the decrease in transmittance at higher Zr doping amounts might occur for the following reasons: (1) a scattering of photons by crystal defects created by doping. This is in good agreement with the AFM topography; thus, the surface roughness of the films was found to decrease as the Zr concentration increased. (2) As the Zr concentration into SnO_2 increased, the structural lattice sites of SnO_2 were disturbed, and the number of defects increased in the lattice sites. This is in good agreement with the XRD pattern, in which a peak shift was found.

The absorption coefficient (α) is determined by the following equation [34]:

$$\alpha = \frac{\ln\left(\frac{1}{T}\right)}{t}, \tag{5}$$

where T is the transmittance, and t is the thickness of the film. The optical bandgap of the pure and Zr-doped films can be obtained from transmission measurements using the Wood–Tauc relation [35]:

$$\alpha h\nu = A\left(h\nu - E_g\right)^{\frac{1}{2}}, \tag{6}$$

where $h\nu$ is the photon energy, A is a constant, E_g is the energy bandgap, and E_g values are calculated by plotting $(\alpha h\nu)^2$ vs. $h\nu$ and extrapolating the linear portion of the graph to zero absorption $[(\alpha h\nu)^2 = 0]$, as shown in Fig. 4. It can be noticed that the optical band-gap values continuously decrease as the Zr doping in SnO_2 increases. The band-gap values of the pure SnO_2 (Z0) and Zr-doped SnO_2 films (Z1, Z2, Z3, and Z4) are found to be 3.94, 3.90, 3.88, 3.82, and

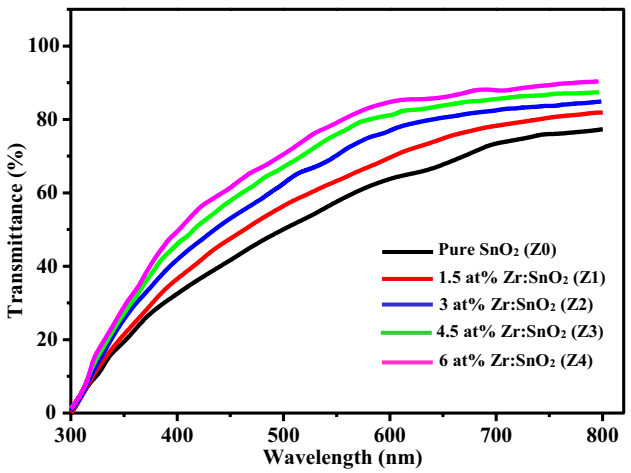

Fig. 3 Optical transmittance vs. wavelength curves of pure SnO_2 (Z0) and various concentrations (1.5, 3, 4.5, and 6 at%) of Zr-doped SnO_2 (Z1, Z2, Z3, and Z4) films

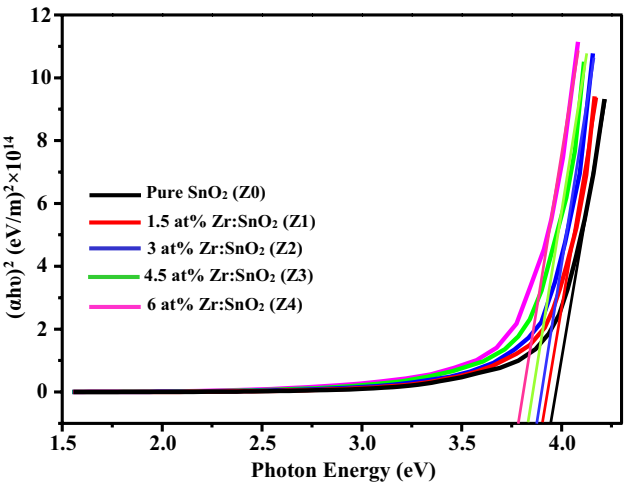

Fig. 4 $h\nu$ (photon energy) vs. $(\alpha h\nu)^2$ curves for pure SnO_2 (Z0) and various concentrations of (1.5, 3, 4.5, and 6 at%) Zr-doped SnO_2 (Z1, Z2, Z3, and Z4) films

3.68 eV, respectively. The decrease in the energy bandgap with Zr doping is probably a result of the formation of new recombination lattice sites in SnO_2 with lower emission energy [36]. This indicates a stoichiometric deviation and degeneracy of Zr-doped SnO_2, and an increase in the number of oxygen vacancies within the lattice.

Electrical properties such as the sheet resistance (R_{sh}) and resistivity (ρ) of the Z0, Z1, Z2, Z3, and Z4 films were measured at room temperature using a four-probe method, which confirmed that all deposited films exhibit *n*-type conductivity. Figure 5 shows the sheet resistance (R_{sh}) vs. the Zr concentration. The R_{sh} values significantly decrease as the Zr concentration increases. The R_{sh} values of Z0, Z1, Z2, Z3, and Z4 are 88.4, 56.3, 32.6, 14.5, and 6.8 Ω, respectively. The measured sheet resistance values are illustrated in Table 1.

The decrease in the sheet resistance of the Zr:SnO_2 films can be attributed to the existence of different valence states of Zr. In the Zr:SnO_2 films, some of the Sn^{+4} ions in the lattice can be replaced by Zr^{+4} ions. This results in a decrease in the sheet resistance, and in this case, Zr acts as a donor. In general, in transparent conducting metal oxide films, the optical transmission and electrical resistance play a vital role in solar-cell applications. In the present study, the Zr-doped SnO_2 films exhibited higher optical transmittance and lower sheet resistance. Therefore, these films are potential candidates for solar-cell window materials.

The corresponding resistivity (ρ) values were also measured for all deposited films, and the values are given in Table 1. The ρ values decrease as the Zr concentration increases, followed by the sheet resistance (R_{sh}) values. To determine the efficiency of the pure SnO_2 (Z0) and Zr-doped SnO_2 (Z1, Z2, Z3, and Z4) films, we measured the figure-of-merit parameter using the Haacke equation [37]:

$$\phi = \frac{T^{10}}{R_{sh}}, \tag{7}$$

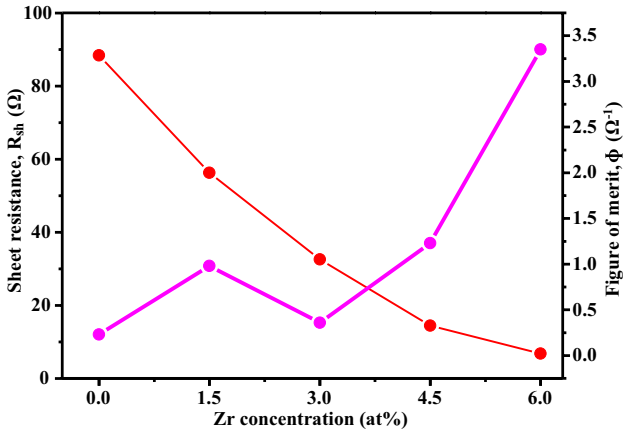

Fig. 5 Sheet resistance and figure-of-merit values with function of Zr (0, 1.5, 3, 4.5, and 6 at%) concentration

where T is the transmittance at 650 nm, and R_{sh} is the sheet resistance. The calculated value of the figure of merit vs. the Zr doping concentration is depicted in Fig. 5. It can be observed that the figure of merit increases significantly as the Zr doping concentration increases in the SnO_2 films. A higher figure-of-merit value is obtained in Z4 (6-at% Zr:SnO_2) film. These findings are indicating that the deposited Zr-doped SnO_2 films are very useful for solar-cell and optoelectronic device applications.

4 Conclusion

We successfully deposited pure SnO_2 and Zr-doped SnO_2 thin films onto glass substrate using a spray pyrolysis technique. The effects of adding Zr on the structural, electrical, and optical properties were investigated. The XRD pattern revealed that all deposited films were crystalline with a preferred orientation of (200) and exhibited a polycrystalline tetragonal rutile structure. SEM and AFM images showed that the grains of all deposited films were spherical in structure, and the grain size effectively changed with the Zr concentration. The optical properties were confirmed that the average optical transmittance was > 85% of the Zr-doped SnO_2 films. The measured optical band-gap value decreased from 3.94 to 3.68 eV as the Zr concentration increased. Furthermore, electrical properties such as the sheet resistance (R_{sh}) and resistivity (ρ) of the SnO_2 films decreased with Zr doping. The lowest values of $R_{sh} = 6.82$ Ω and $\rho = 0.4 \times 10^{-3}$ Ω-cm were obtained in 6-at% Zr-doped SnO_2 film. Consequently, a good efficiency value of the figure of merit ($\phi = 3.35 \times 10^{-3}$ Ω^{-1}) was found in 6-at% Zr-doped SnO_2 film. These substantial properties of Zr-doped SnO_2 films make them useful for wider optoelectronic device applications.

Acknowledgements Author Dr. N. Nanda Kumar Reddy thankfully acknowledges the Management of Madanapalle Institute of Technology and Science (MITS, Madanapalle) for providing the financial support through MITS/TEQIP-II/FACULTY-SEED GRANT/16–17/20. We thank to Dr. Madhukar Poloju, Department of Physics, Osmania University, Hyderabad for useful discussions and technical support.

References

1. P. Docampo, H.J. Snaith, Nanotechnology **22**, 225403 (2011)
2. A. Espinosa, N. Sánchez, J. Sánchez-Marcos, A. de Andrés, M.C. Muñoz, J. Phys. Chem. C **115**, 24054 (2011)
3. H.X. Li, Q.Q. Wei, Y.Y. Liu, K. Wu, Adv. Mater. Res. **465**, 198 (2012)
4. L. Chen, F. Wu, Micro Nano Lett. IET **7**, 248 (2012)
5. H.R. Kim, A. Haensch, I.D. Kim, N. Barsan, U. Weimar, J.H. Lee, Adv. Funct. Mater. **21**, 4456 (2011)
6. X. Dou, D. Sabba, N. Mathews, L.H. Wong, Y.M. Lam, S. Mhaisalkar, Chem. Mater. **23**, 3938 (2011)

7. D.K. Pham, N. Barsan, U. Weimar, Sens. Actuators B Chem. **158**, 388 (2011)
8. A.M.E. Sayed, S. Taha, M. Shaban, G. Said, Superlattices Microstruct. **95**, 1 (2016)
9. H.A. Mohamed, Optoelectron Adv. Mater. Rapid Commun. **3**, 936 (2009)
10. A. Antonaia, P. Menna, L.M. Addonizio, M. Crocchiolo, Sol. Energy Mater. Sol. Cells **28**, 167 (1992)
11. M.M.B. Mohagheghi, M.S. Saremi, J. Phys. D Appl. Phys. **37**, 1248 (2004)
12. R. Singh, M. Kumar, S. Shankar, R. Singh, A.K. Ghosh, O.P. Thakur, B. Das, Mater. Sci. Semicond. Process **31**, 310 (2015)
13. H.R. An, C.Y. Kim, S.T. Oh, H.J. Ahn, Ceram. Int. **40**, 385 (2014)
14. A. Benhaoua, A. Rahal, B. Benhaoua, M. Jalaci, Superlattices Microstruct **70**, 61 (2014)
15. G. Turgut, E.F. Keskenler, S. Aydın, E. Sönmez, S. Dogan, B. Düzgün, M. Ertugrul, Superlattices Microstruct. **56**, 107 (2013)
16. C. Sankar, V. Ponnuswamy, M. Manickam, R. Mariappan, R. Suresh, Appl. Surf. Sci. **349**, 931 (2015)
17. T.I. Gandhi, R.R. Babu, K. Ramamurthi, M. Arivanandhan, Thin Solid Films **598**, 195 (2016)
18. G. Li, X. Fang, W. Feng, J. Liu, J. Alloys Compd. **716**, 106 (2017)
19. D.S. Han, J.H. Park, Y.J. Kang, J.W. Park, Microelectron. Reliab. **53**, 1875 (2013)
20. A. Juma, I.O. Acik, A.T. Oluwabi, A. Mere, V. Mikli, M. Danilson, M. Krunks, Appl. Surf. Sci. **387**, 539 (2016)
21. A.F. Khan, M. Mehmood, M. Aslam, M. Ashraf, Appl. Surf. Sci. **256**, 2252 (2010)
22. H.P. Dang, Q.H. Luc, V.H. Le, T. Le, J. Alloys Compd. **687**, 1012 (2016)
23. D.K. Lee, Z. Wan, J.S. Bae, H.B.R. Lee, J.H. Ahn, S.D. Kim, J. Kim, S.H. Kwon, Mater. Lett. **166**, 163 (2016)
24. Y.M. Lu, J. Jiang, M. Becker, B. Kramm, L. Chen, A. Polity, Y.B. He, P.J. Klar, B.K. Meyer, Vacuum **122**, 347 (2015)
25. G.W. Kim, C.H. Sung, M.S. Anwar, Y.J. Seo, S.N. Heo, K.Y. Park, T.K. Song, B.H. Koo, Curr. Appl. Phys. **12**, S21 (2012)
26. A.R. Babar, S.S. Shinde, A.V. Moholkar, C.H. Bhosale, J.H. Kim, K.Y. Rajpure, J. Alloy. Compd. **505**, 416 (2010)
27. S. Chacko, N.S. Philip, K.G. Gophandran, P. Koshy, V.K. Vaidyan, Appl. Surf. Chem. **254**, 2179 (2008)
28. B.D. Cullity, *Elements of X-ray diffraction*, 2nd edn, vol. 99. (Addison-Wesley publishing company Inc., Philippines, 1978)
29. M. Bedir, M. Öztas, O.F. Bakkaoglu, R. Ormanel, Eur. Phys. J. B **5**, 465 (2005)
30. M. Dhanam, P.K. Manoj, R. Rajeev, R. Prabhu, J. Cryst. Growth **280**, 425 (2005)
31. H.S. Akkera, D. Kaur, Appl. Phys. A **122**, 1 (2016)
32. S.S. Lekshmy, K. Joy, J. Mater. Sci. Mater. Electron **25**, 1664 (2014)
33. H.S. Akkera, I. Singh, D. Kaur, J. Alloys Compd. **642**, 53 (2015)
34. J. Tauc, R. Grigorovici, A. Vancu, Phys. Status Solidi B **15**, 627 (1966)
35. J. Tauc (ed.), (Academic Press, New York, 1966), p. 277
36. B. Xu, X.G. Ren, G.R. Gu, L.L. Lan, B.J. Wu, Superlattices Microstruct. **89**, 34 (2016)
37. G. Haacke, J. Appl. Phys. **47**, 4086 (1976)